journal

J. Am. Ceram. Soc., 89 [2] 431–437 (2006)
DOI: 10.1111/j.1551-2916.2005.00763.x

Two-Step Sintering of Ceramics with Constant Grain-Size, I. Y_2O_3

Xiao-Hui Wang*, Pei-Lin Chen, and I-Wei Chen†

Department of Materials Science and Engineering, University of Pennsylvania, Philadelphia, Pennsylvania 19104

Isothermal and constant-grain-size sintering have been carried out to full density in Y_2O_3 with and without dopants, at as low as 40% of the homologous temperature. The normalized densification rate follows Herring's scaling law with a universal geometric factor that depends only on density. The frozen grain structure, however, prevents pore relocation commonly assumed in the conventional sintering models, which fail to describe our data. Suppression of grain growth but not densification is consistent with a grain boundary network pinned by triple-point junctions, which have a higher activation energy for migration than grain boundaries. Long transients in sintering and grain growth have provided further evidence of relaxation and threshold processes at the grain boundary/triple point.

I. Introduction

Sintering is a complicated process of microstructure evolution, with the main outcome being porosity elimination.[1–4] However, in polycrystals accelerated grain growth is also reckoned to always accompany final-stage sintering. The onset of accelerated grain growth depends on the microstructure; a uniform size and shape distribution of pores and grains postpones accelerated grain growth.[5,6] In the best case the onset can be postponed to about $\rho = 92\%$ which, for most ceramics with a dihedral angle of 120°, coincides with the Rayleigh transition when pore channels collapse to become isolated pores.[7–9] Such collapse results in a substantial decrease in pore pinning, which triggers accelerated grain growth.[10,11] The prevailing sintering paradigm in the last 40 years is to mitigate this undesirable outcome by suppressing grain boundary mobility while promoting pore pinning. The aim is to maintain pore-grain boundary contact during grain growth so that pore breakaway never occurs.

Contrary to the above paradigm, we have used a simple two-step sintering method to sinter Y_2O_3, from 75% to 100% density, without grain growth.[12] The key elements in this method are (a) reaching a higher temperature T_1 to conduct first-step sintering, (b) achieving a high-density ρ^* at T_1; $\rho^* \geq 75\%$ to render pores unstable,[13] and (c) lowering the temperature to T_2 to conduct second-step sintering during which there is only densification and no grain growth. The purpose of the present paper is to analyze in detail the sintering kinetics of Y_2O_3, a model system, in order to shed light on the sintering mechanism. The relevance of the present work to low-temperature kinetics and nanograin ceramics will also be explored. In addition to Y_2O_3, this method has been successfully applied to $BaTiO_3$ and Ni–Zn ferrite, which densify by solid-state diffusion, as shown in the companion paper.[14] It also succeeded in liquid-phase-containing ceramics, ZnO and SiC, as reported in the recent literature.[15,16]

Analysis of sintering data requires a sound physical model. Although theoretical models usually use idealized geometric assumptions which may not hold in real materials,[8,10,11,17–26] a general dimensional argument originated by Herring[27,28] states that the normalized rate of densification, via grain boundary diffusion, can be expressed as

$$\frac{d\rho}{\rho dt} = F(\rho)\frac{3\gamma\Omega}{kT}\frac{\delta D}{G^4} \quad (1)$$

Here t is the time, γ the surface energy, Ω the atomic volume, k the Boltzmann constant, T the absolute temperature, G the mean grain diameter, δ the width of the grain boundary, D the grain boundary diffusivity, and $F(\rho)$ an unspecified function of density ρ. This argument holds for different grain size and density provided the sintering microstructure, including the pore distribution, is a function of density only once the length scale is renormalized by the grain size. For a ceramic undergoing two-step sintering, the grain boundary network is frozen, so there is no change in microstructure other than the shrinking porosity. This would seem to satisfy Herring's assumption. Therefore, we will attempt to use Eq. (1) in our analysis.

Various models of intermediate and final-stage sintering have specified the function $F(\rho)$. Typically, at $\rho > 0.7$, the predicted $F(\rho)$ is a gradual, decreasing function of ρ, which was supported by the data of Hansen *et al.*[26] On the other hand, Zhao and Harmer[29] found, after accounting for grain-size increase, a $F(\rho)$ that slightly increased with density in final-stage sintering. They attributed the increase to the increased number of pores that intersect a typical grain boundary as sintering proceeds. Cameron and Raj,[5] however, found qualitative disagreement between their data and all the geometrical models they examined. Instead, an empirical model that depicts densification as an exhaustion process seemed to fit their data the best.

The attainment of constant grain size throughout intermediate and final-stage sintering in second-step sintering offers an excellent opportunity to verify Eq. (1) and evaluate $F(\rho)$, which is a main objective of our work. Once Eq. (1) is confirmed, any deviation of the experimental data from the expected behavior of Eq. (1) would imply important changes in the underlying sintering kinetics.

II. Experimental Procedure

(1) Powder Preparation

The Y_2O_3 powders were synthesized by a standard solution-polymerization route using yttrium nitrate ($Y(NO_3)_3$, Alfa, New York, NY) and polyethylene glycol (PEG, FW = 2000, Alfa) as raw materials. The polymeric precursor for the Y_2O_3 was prepared by mixing an appropriate amount of nitrate salt and PEG into distilled water. After heating and stirring at 80°C, a transparent aqueous precursor solution was obtained. The precursor solution was then heated until the solution evaporated, leaving a soft, light brown, aerated gel. The dried gel was ground with an agate mortar and pestle, then calcined in air at various temperatures to obtain Y_2O_3 powders with different particle sizes in the range of 10–60 nm.

M. Harmer—contributing editor

Manuscript No. 20592. Received May 23, 2005; approved August 8, 2005.
This work was supported by the U.S. National Science Foundation, Grant Nos. DMR03-03458 and DMR05-20020, and by the Ministry of Sciences and Technology of China through 973-project under grant 2002CB613301 and 863-project under grant 2001AA325010.
*State Key Laboratory of New Ceramics and Fine Processing, Department of Materials Science and Engineering, Tsinghua University, Beijing, China.
†Author to whom correspondence should be addressed. e-mail: iweichen@upenn.edu

Mg^{2+} and Nb^{5+} were used as cation dopants substituting Y at 1 at.%. First, Y_2O_3 powders were dispersed in isopropyl alcohol. A solution containing $Mg(NO_3)_2$ was then added into the Y_2O_3 dispersion and the slurry was flocced by increasing the pH using NH_4OH. The flocced material was dried and later calcined in air at 600°C for 2 h to yield a uniform MgO coating on Y_2O_3 particles. For Nb doping, an (isopropyl) alcohol dispersion of Y_2O_3 was first mixed with a solution of niobium isopropoxide, and the mixture was next hydrolyzed by adding deionized water at room temperature. The slurry was dried and calcined at 600°C for 2 h. To avoid SiO_2 contamination, powder processing was conducted using plastic ware only, and sintering was performed using a dedicated "clean" furnace.

(2) Powder Compacts and Sintering

Pellets (diameter = 10 mm, thickness = 10 mm) were prepared by die pressing followed by cold isostatic pressing. Pressure up to 310 MPa was applied to obtain green bodies with different densities. Subsequent sintering was conducted in air.

(A) Normal Sintering: Normal sintering up to 1600°C used a constant heating rate of 10°C/min. After reaching the desired temperature, the power was turned off to allow samples to cool naturally in the furnace. The specimen dimensions were measured *in situ* during heating in a lateral dilatometer using dense alumina as a reference. Isotropic shrinkage was found, which allows the density to be calculated from the current length and the final density measured by the Archimedes method. Density data are presented in fraction or percentage of the theoretical density, taken as 5.013 mg/m^3 for Y_2O_3.

(B) Two-Step Sintering: In two-step sintering, the sample was first heated at 10°C/min to T_1, then cooled at 50°C/min to T_2 and held there from 6 to 30 h. This schedule was chosen to minimize densification during heating and cooling transients. Runs interrupted after the first step or during the second step were performed in order to examine intermediate microstructure. The specimen dimensions were also measured *in situ* throughout two-step sintering using the same dilatometer.

(3) Characterization

Initial particle size was determined using transmission electron microscopy, scanning electron microscopy (SEM) and X-ray diffraction. In the Archimedes method for density measurements for samples with only closed porosity, distilled water was used as the displacement fluid and the estimated accuracy was within ± 0.01 g/cm^3. For each experiment, the average density of three pellets was used in the analysis (their densities were within $\pm 2\%$ of each other). For samples with open porosity, such as after first-step sintering, the density was estimated from the weight and dimension of duplicate specimens; the estimates were consistent with the data of dilatometry. Microstructures of sintered compacts were observed in an SEM using specimens that were either fractured, or polished and then thermally etched. At lower densities, the mean grain (particle) size was estimated on the fracture surface. At higher densities, the grain size was obtained by multiplying the average linear intercept length of at least 500 grains by 1.56.

Dihedral angles were determined using samples sintered in a previous study from a coarse powder (200 nm).[27–29] These samples had a density of around 85%–90%, and they were subjected to long annealing at low temperatures to develop the dihedral angles between pores and grain boundaries. At least 200 dihedral angles were measured for each material to obtain a statistical distribution.

III. Results and Data Analysis

(1) Microstructure of Two-Step Sintering

We have previously published the microstructure of two-step sintered Mg^{2+}-doped Y_2O_3 using powders with an initial particle size of 10 nm and a final dense ceramic grain size of 60 nm.[12]

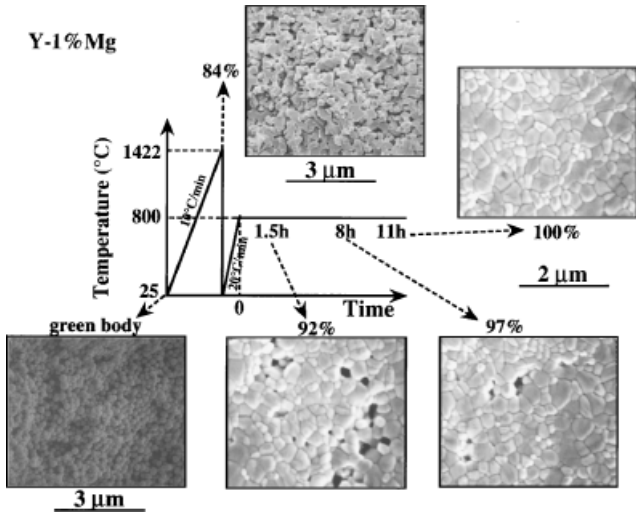

Fig. 1. Summary of two-step sintering experiment using Y_2O_3 (with 1% Mg^{2+}) starting with spherical powders of a particle size 200 nm. No grain growth (grain size 390 nm) was observed in the second step.

The temperatures used were 1080°C for T_1 and 1000°C for T_2. To contrast this observation, we here show the microstructure of a set of coarser ceramics obtained by two-step sintering using powders of a much larger size, 200 nm.[30] These powders were prepared by a homogeneous precipitation method using urea to assist precipitation.[31] They were spherical in shape and doped with 1% Mg^{2+}. Two-step sintering was conducted using (1) 10°C/min heating to T_1 (1422°C) to gain a density of 84%, followed by cooling, and (2) reheating at 20°C/min to T_2 (800°C) for 11 h to gain full density. Microstructures of the green body after first-step sintering, and at various time during second-step sintering, are shown in Fig. 1 to demonstrate the absence of grain growth at T_2. Throughout the second step a constant grain size of 390 nm was maintained, which is about twice the size of the starting powder. We are not aware of any other sintering method that resulted in a less coarsened microstructure, from starting powder size to dense ceramic grain size, than that in Fig. 1. Using similar two-step sintering methods, we were able to densify a Nb^{5+}-doped Y_2O_3 without grain growth in the second step, starting with a 200 nm powder and reaching a final grain size of 400 nm (data not shown.)

These experiments were initially conducted to search for an appropriate (T_2) temperature suitable for thermal etching of partially dense Y_2O_3 in order to reveal dihedral angles between pores and grain boundaries. Many such experiments yielded ceramics that continued to densify at T_2, eliminating most or all the pores. From these experiments we concluded that T_2 sintering was feasible for Y_2O_3 of a grain size of 60–400 nm. In $BaTiO_3$ and Ni–Zn ferrite, constant grain size sintering in the 70–800 nm range was also demonstrated as shown in the companion paper.[14]

Measured dihedral angles for undoped and doped Y_2O_3 are shown in Fig. 2. They are around 110° regardless of dopants. Therefore, doping is not likely to cause a systematic difference in the microstructure. In particular, the critical size ratio of a pore to neighboring grains that renders the pore thermodynamically unstable[13] in Y_2O_3 is likely to be similar regardless of dopants. These results justify the use of the same $F(\rho)$ in the following analysis.

(2) $F(\rho)$ as a Universal Function

The densification curves during T_2 sintering are described next. Figure 3 shows five sets of data from runs that had no grain growth, although they varied in composition, sintering temperatures (T_1 and T_2), and starting grain size at T_2. According to Eq. (1), if the function F depends on density only, then these

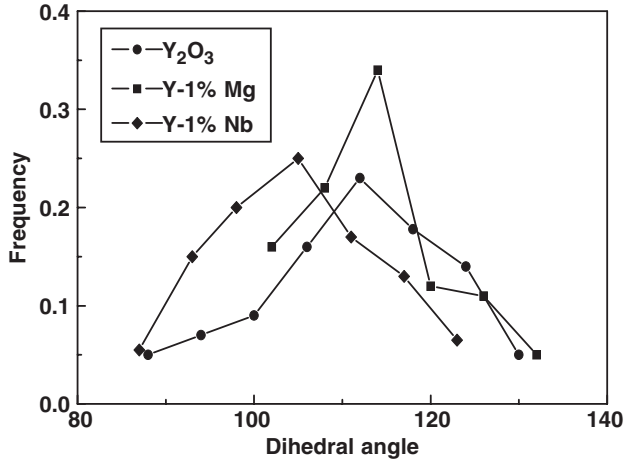

Fig. 2. Dihedral angles of undoped and doped Y_2O_3.

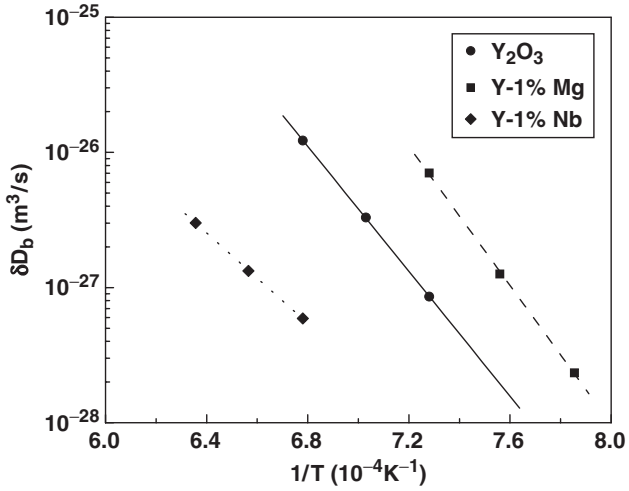

Fig. 4. Estimated grain boundary diffusivity against reciprocal temperature.

data, plotted in a semi-log form, should fall on curves that are vertically parallel to each other. This is indeed the case.

By plotting normalized densification rate against grain size in a log–log form (not shown), we obtained an exponent of 3.7, which is close to four used in Eq. (1). The normalized densification rate was further used to determine the activation energy of grain boundary diffusion, by rewriting Eq. (1) into

$$\delta D = \frac{\mathrm{d}\rho}{\rho\,\mathrm{d}t}\frac{1}{F(\rho)}\frac{kT}{3\gamma\Omega}G^4 \tag{2}$$

The obtained activation energies are listed in Table I and compared with the data in the literature. These grain size exponent and activation energies are essentially independent of the density used in the data analysis, which is consistent with the assumption that $F(\rho)$ is a universal function.

According to Hansen *et al.*,[26] the value of $F(\rho)$ varies very slightly between $\rho = 0.75$ and 0.85 and is around 12 000 at $\rho = 0.8$. (Here we need to account for a factor three to convert length measurement to density measurement.) Accepting these values, we estimated the grain boundary diffusivity and showed it in Fig. 4. In the above estimate, we have assumed γ to be 1 J/m^2 and Ω 7.74×10^{-29} m^3 in Eq. (2). The δD_0 determined for Y_2O_3 is $(2.36 \pm 0.40) \times 10^{-12}$ m^3/s; for Y_2O_3 doped with Mg^{2+} and Nb^{5+}, δD_0 are $(1.08 \pm 0.15) \times 10^{-6}$ and $(5.79 \pm 0.11) \times 10^{-17}$ m^3/s, respectively. These values are comparable with those determined from grain boundary mobilities using grain growth data at higher temperatures (see Table I).[32,33]

(3) Kinetic Window for Constant Grain Size Sintering

If second-step sintering was conducted at too low a temperature (T_2), sintering proceeded for a while (typically for 5%), then became exhausted. The normalized densification rates in Fig. 5 (curves A–C) fall below what is expected from $F(\rho)$, starting at about $\rho = 0.85$. As there was no grain growth at T_2, the slow-down may be attributed to grain boundary diffusion that also became exhausted. At higher T_2, grain growth was observed during second-step sintering. The normalized sintering rates again fall below what is expected from $F(\rho)$, as is also shown in Fig. 5 (curves D–F), at $\rho > 0.85$. This slow-down is because of increasing grain size.

The temperature (T_2) and the grain size of various samples that successfully underwent second-step sintering to reach full density (at least 99% in this paper) without grain growth are marked in Fig. 6 using solid symbols. They are bordered by two lines which delineate the "kinetic window." The open symbols below the lower boundary line are experiments that showed no grain growth but densification was exhausted; the open circles above the upper boundary line are ones in which grain growth occurred. For each of the latter data, we also draw a horizontal arrow that points to the final grain size when full density was reached. It seems reasonable that all the arrows end at the upper boundary line, as once within the "kinetic window" the grain size should stop growing. A partial list of the successful two-step sintering experiments (reaching nearly full density without grain growth) is given in Table II. It is clear that the lowest T_2 required to reach full density was much lower than those reported in the

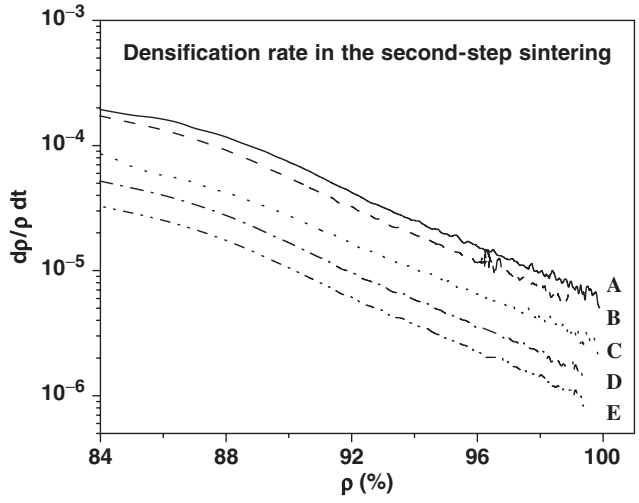

Fig. 3. Normalized densification rates during second-step sintering without grain growth. Samples were heated to T_1 (the first temperature given below) then cooled to T_2 (the second temperature given below) and held for the time specified. The grain size during T_2 sintering is also specified (in parentheses). A, Y_2O_3, 1250°, 1150°C—20 h (122 nm); B, Y_2O_3, 1310°, 1150°C—20 h (140 nm); C, Y_2O_3 (1% Nb^{5+}), 1450°, 1200°C—40 h (118 nm); D, Y_2O_3, 1310°, 1100°C—30 h (140 nm); E, Y_2O_3 (1% Mg^{2+}), 1250°, 1050°C—30 h (116 nm).

Table I. Activation Energy for Grain Boundary Diffusion of Y_2O_3

	Activation energy (KJ/mol)	
Sample	Present results	Reference results
Y_2O_3	410	340,[30] 398[29]
Y–1% Mg	553	636[29]
Y–1% Nb	310	272[29]

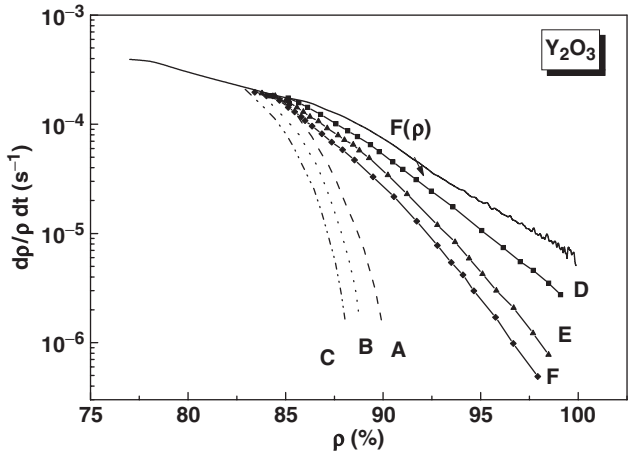

Fig. 5. Normalized densification rate of Y_2O_3 samples in second-step sintering. Curves are shifted vertically for easy comparison with the universal density function $F(\rho)$. Same notation as in Fig. 3. No grain growth was observed but densification was incomplete in A, 1310°, 1000°C—10 h; B, 1250°, 1000°C—10 h; and C, 1250°, 950°C—10 h. Grain growth was observed in D, 1310°, 1300°C—10 h; E, 1310°, 1250°C—10 h; and F, 1310°, 1200°C—10 h.

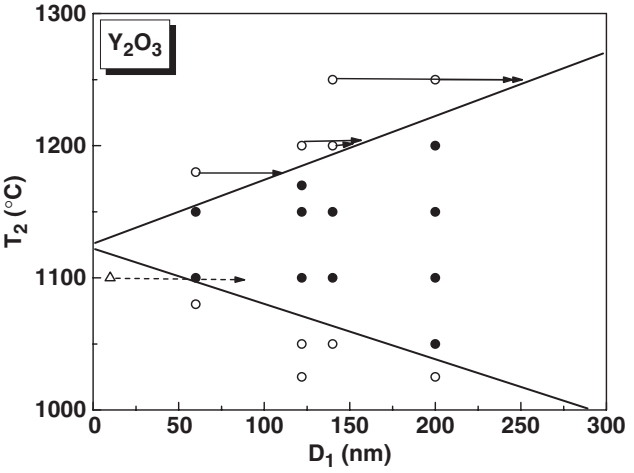

Fig. 6. Temperature (T_2) and grain size used for second-step sintering in Y_2O_3. Solid symbols are ones reaching full density without grain growth; open symbols did not. Data above the upper boundary had grain growth (arrow from initial to final grain size); data below the lower boundary did not fully densify. Triangle represents a one-step sintering experiment at the temperature shown, with grain size starting at the triangle and growing to the arrowhead, when full density was reached.

literature.[32,33] Note that the lowest density after T_1 in this table is 75%, which is the critical density ρ^* expected for pores with a dihedral angle of 110°–120° to become unstable.[12] (Runs of lower starting density did not reach full density at T_2, and thus are not included in Table II.)

The "kinetic window" is, to some extent, history dependent and, thus, not unique. If the powder compact is directly sintered at an intermediate temperature without pre-firing at the higher temperature (T_1), it follows a somewhat different trajectory. This is illustrated by the case where 10 nm powders were used to conduct one-step, isothermal sintering at 1100°C, indicated by the open triangle in Fig. 6. This sample sintered to full density but also experienced considerable grain growth, bringing the final grain size to where the broken arrow points to. Pre-firing at T_1 is therefore important for suppressing grain growth at T_2.

Fully dense samples did not resist grain growth indefinitely at T_2. As shown in Fig. 7, the grain size increased after a long incubation time. The grain growth curve is concave upward, which is highly unusual because the typical (parabolic) grain growth curve has a concave downward shape.[32,34] As the driving force for grain growth diminishes with time, the upward curvature must reflect an increase in grain boundary mobility with time, which, again, is a highly unusual observation.

(4) Mg and Nb Doping

The normal sintering and grain growth curves of three 30 nm powders, Y_2O_3, Mg-doped Y_2O_3, and Nb-doped Y_2O_3 are displayed in Fig. 8 for comparison. Here, the highest temperature reached was 1500°C for Y_2O_3, 1350°C for the Mg-doped sample, and 1600°C for the Nb-doped sample. They clearly show that, at higher temperatures, Mg enhances kinetics while Nb does the opposite. At lower temperature, less shrinkage in the Mg-doped sample is because of greater extent of coarsening in the powder (not shown). This coarsening occurs during calcination (600°C for 2 h), and it proceeds by surface diffusion which Mg-doping also promotes.[35]

The effect of Mg and Nb doping in two-step sintering parallels that in normal sintering and grain growth. This is evident in Table II in which T_2 is clearly lower for Mg-doped samples than undoped samples. The opposite effect is seen for Nb doping. The "kinetic windows" of constant grain-size sintering at T_2 are outlined for doped Y_2O_3 in Fig. 9. Compared with Fig. 6 for undoped Y_2O_3, these windows are shifted in temperature to reflect the enhanced/depressed kinetics because of doping. As before, the arrows in Fig. 6 indicate the extent of grain growth at higher temperatures. Again, the arrows end at the upper boundary of the "kinetic window." We also show, by triangles, two doped samples of 10 nm powders, sintered in one step at intermediate temperatures. As they have a substantially different

Table II. Two-Step Sintering of Y_2O_3 (30 nm Powders)

		After first-step sintering				After second-step sintering			
Sample	ρ_0 (%)	T_1 (°C)	t_1 (h)	ρ_1 (%)	G_1(nm)	T_2 (°C)	t_2 (h)	ρ_2 (%)	G_2 (nm)
Y_2O_3-1	44	1250	0	75	122	1150	20	99.5	125
Y_2O_3-2	44	1250	0	75	122	1100	30	99.0	123
Y_2O_3-3	44	1310	0	80	138	1150	20	99.6	140
Y_2O_3-4	44	1310	0	80	138	1100	30	99.6	140
Y_2O_3-5	44	1350	0	85	160	1150	20	99.5	165
Y_2O_3-6	44	1350	0	85	160	1100	30	99.0	162
Y_2O_3-7	44	1400	0	88	200	1150	20	99.5	202
Y_2O_3-8	44	1400	0	88	200	1050	40	99.0	196
Y–1%Mg-1	44	1250	0	78	116	1100	20	100	120
Y–1%Mg-2	44	1250	0	78	116	1050	30	100	118
Y–1%Mg-3	44	1300	0	84	155	1050	20	100	157
Y–1%Mg-4	44	1300	0	84	155	1000	20	100	160
Y–1%Nb-1	44	1450	0	82	115	1250	20	99.2	120
Y–1%Nb-2	44	1450	0	82	115	1200	40	99.0	118

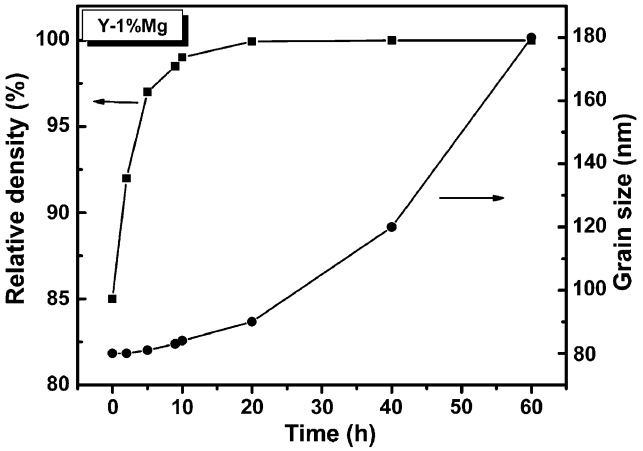

Fig. 7. Density and grain size of Y_2O_3 (with 1% Mg^{2+}) sintered in the second step at 1000°C for 60 h. Sample previously preheated to 1120°C (T_1) without holding.

thermal history, their grain size trajectories were again not bounded by the boundary lines.

IV. Discussion

To achieve densification without grain growth, grain boundary diffusion needs to be maintained while grain boundary migration is suppressed. It is well known that the kinetics of these two processes are decoupled when solute drag of the grain boundary is involved, because the latter entails lattice diffusion that has a higher activation energy. Indeed, solute drag is an effective strategy for controlling abnormal grain growth in final-stage sintering.[2] In our case, however, solute drag cannot be a significant factor as the same phenomena were also observed in (Mg)-doped samples that showed enhanced grain boundary kinetics. We previously suggested that another drag mechanism, because of relatively immobile triple points (including three-grain junction lines, four-grain junction points and their equivalent involving grain/pore junctions), may provide a decoupling mechanism.[10,11] This idea is schematically sketched in Fig. 10 that delineates the grain boundary mobility M_b and junction mobility M_j, assuming the latter has a higher activation energy. The mobility of the grain boundary network, which is required to allow grain growth in a polycrystal, is given by $(M_b^{-1}+M_j^{-1})^{-1}$. Therefore, the network mobility follows the grain boundary mobility at high temperature and junction mobility at low temperature, and below the temperature when $M_b \sim M_j$ it is essentially frozen despite considerable grain boundary diffusion. Direct observation of triple point drag has been reported by Czubayko *et al.* in high purity zinc tricrystals at low temperature.[36,37] They found the moving grain boundaries maintained a (triple-point) dihedral angle $<120°$ in order to exert a force on the grain junction to pull it forward. At higher temperatures, the dihedral angle reverted to 120°, indicating little triple-point drag. The same drag could occur in our samples at T_2. Meanwhile, as densification does not involve grain boundary migration, it still proceeds via grain boundary diffusion.

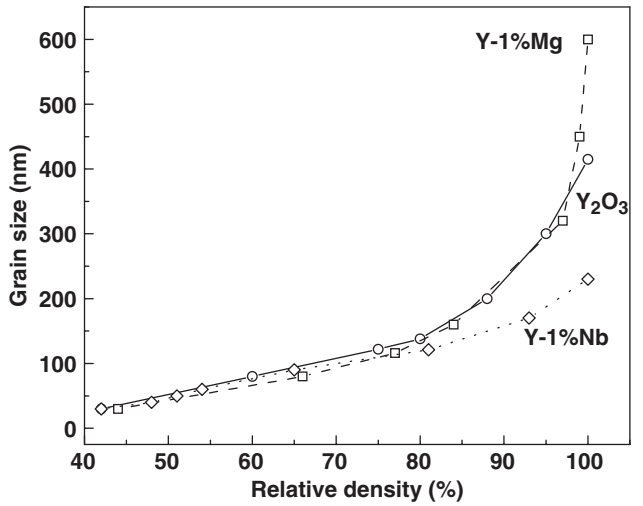

Fig. 8. Density and grain size during heating (10°C/min) of undoped and doped Y_2O_3. Initial powder size = 30 nm. See text for highest temperature reached.

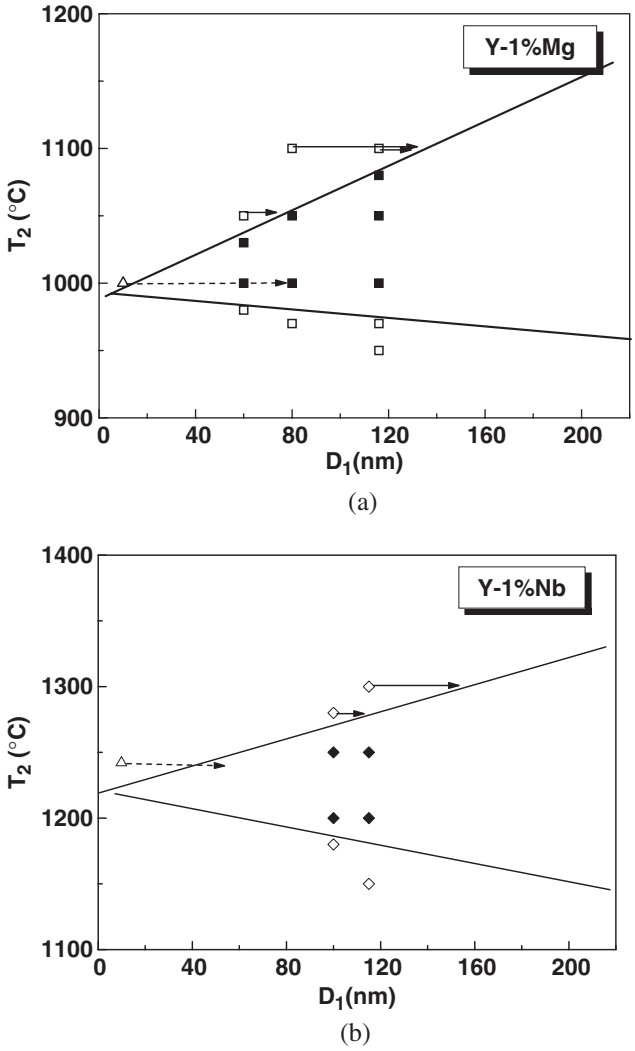

Fig. 9. Maps for second-step sintering for Y_2O_3 with 1% Mg^{2+} (squares) and Y_2O_3 with 1% Nb^{5+} (diamonds). Same notation as in Fig. 6.

The crossover depicted in Fig. 10 and the kinetic windows shown in Figs. 6 and 9 provide helpful guides to experimental design but are probably not unique in view of the evidence of history dependence and thermal hysteresis/transisent in our study. Such evidence includes (a) slowdown and exhaustion of diffusion at low temperature, (b) incubation time for grain growth to initiate after constant grain-size sintering, and (c) thermal history dependence of the kinetic window. This may be caused by the slow equilibration of defect configurations on the grain boundaries, pore surface, and pore/grain junctions at low temperatures. Therefore, at intermediate times, long transients and possibly metastable states may reign. Meanwhile, pre-firing at T_1 may have locked pore/grain junctions into stable configurations that are not kinetically accessible at T_2, and the grain

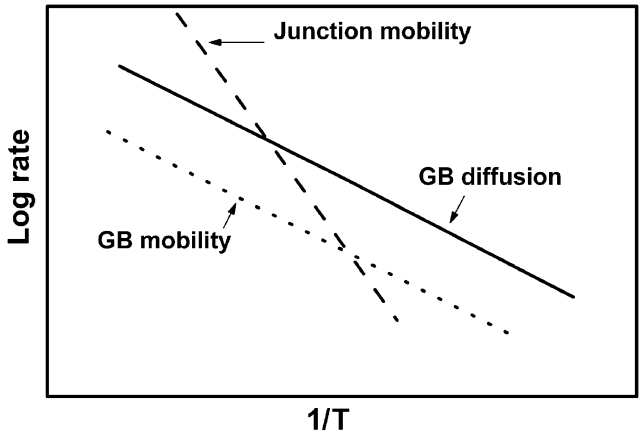

Fig. 10. Schematic Arrhenius plot for grain-boundary diffusion, mobility of pore/grain-boundary junction or four-grain junction, and intrinsic mobility of grain boundary (without drag) which is parallel to grain-boundary diffusion.

boundary movement may entail the transition states of these configurations that have activation barriers insurmountable at T_2. As a result, pre-firing at T_1 followed by sintering at T_2 may enhance the pinning effects and make possible constant-grain-size sintering.

Another possible reason that a higher T_1 is required for two-step sintering is the different sintering mechanisms below and above the critical density. Below the critical density, particle coarsening and repacking (not unlike that in liquid-phase sintering) are the mechanisms responsible for densification,[35] because otherwise the pores should grow as expected from the theory of Kingery and Francois.[13] Although particle coarsening is achieved by surface diffusion, which typically has a lower activation energy than grain boundary diffusion, some repacking events could require more robust kinetics available only at a higher temperature. If so, a higher T_1 would be needed. On the other hand, once the critical density is reached, grain boundary diffusion alone is sufficient to cause densification even if the microstructure is frozen, as illustrated by our experiments. Therefore, a lower T_2 will suffice as long as it is not too low to exhaust diffusion.

The temperature range in the kinetic windows depicted in Figs. 6 and 9 widens with grain size. This shape has also been observed in $BaTiO_3$ and Ni–Zn ferrite,[14] suggesting that it is a general feature for T_2 sintering. If so, we may conclude that a larger grain size may postpone the exhaustion of diffusion at lower T_2 and the non-parabolic grain growth at higher T_2. As the driving force for grain growth decreases with grain size, the delay of grain growth by increasing grain size is reasonable. Meanwhile, the delay of diffusion exhaustion by increasing grain size is consistent with the common notion that grain boundary diffusion may be limited by source/sink actions (e.g., kinks and ledges required to provide and accommodate atoms and point defects) at small grain sizes.[38–41] As diffusion proceeds, some of these kinks and ledges are eliminated by migrating atoms/point defects; after that diffusion may be exhausted if sources/sinks are not replenished by fresh nucleation. The size effects on nucleation are well known; for example, a source/sink in the form of a screw dislocation loop entails a nucleation energy that is inversely proportional to the grain size, so that a threshold stress on the order of $2\gamma/G$, amounting to 20 MPa for a grain size of 100 nm, is obtained. Such sluggish kinetics for source/sink nucleation may be eventually overcome after a long incubation time. According to Fig. 7, this requires 10 h at 1000°C with Mg as "sintering aid." Such a long incubation time is not entirely surprising given that Y_2O_3 has a melting point of 2440°C, so most of our T_2 experiments fell below or were around 0.5 of the homologous temperature.

We now return to the universal sintering function $F(\rho)$. Unlike the previous reports of Zhao and Harmer[25] ($\rho > 90\%$) and Hansen *et al.*[26] ($75\% < \rho < 95\%$), our $F(\rho)$ decreases much more rapidly, by a factor of about 4.5 from $\rho = 0.75$ to 0.9, and by another factor of about 10 from $\rho = 0.9$ to 0.99. In contrast, Hansen *et al.* found a decrease of no more than a factor of three in total, and Zhao *et al.* reported a slight increase. Interestingly, our data in Fig. 3 are empirically consistent with an exponential decay, i.e., $F(\rho) \sim \exp(-c\rho)$ where c is a rather large constant, around 24 for $\rho > 0.88$. This form of $F(\rho)$ has been previously noticed by Cameron and Raj.[5] To understand these differences, we note that in normal sintering, the microstructure is constantly refreshed by grain growth, bringing the remaining pores to coalesce and then to relocate at the newly formed four-grain junctions. As a result, the diffusion distance in normal sintering could remain commensurate with the characteristic grain size even as densification progresses. In our experiments, however, the grain boundary network is frozen. Therefore, as pores around smaller grains that have a shorter diffusion distance are removed first, the remaining pores around larger grains that have a longer diffusion distance remain and become dominant. The effective pore spacing thus constantly moves toward the larger-size end of the grain size distribution, which may be responsible for the exponential-like decrease of $F(\rho)$. This decrease is very steep, because an increase in the pore spacing by a factor of two lowers the normalized sintering rate by a factor of 16 according to Herring.[27]

Despite the rapid decrease of $F(\rho)$, constant-grain-size sintering at T_2 still offers the advantage of lower sintering temperature. Using powders of the same initial particle size, the lowest T_2 achieved in our experiments was always lower than the temperature of conventional isothermal sintering. For example, for 30 nm powders, the lowest T_2 successfully used for Y_2O_3 was 1050°–1100°C, whereas isothermal sintering at 1200°C for 10 h was required to reach 99% density. Likewise, for Mg-doped Y_2O_3 at the same initial powder size, the lowest T_2 successfully used was 1000°–1050°C, whereas isothermal sintering at 1100°C for 10 h was required to reach full density. This illustrates the advantage of lowering the sintering temperature to maintain a constant grain size once the critical density is reached. It is also clear that further advances in sintering dense nanograin ceramics may come from using finer powders and/or other processing methods to achieve the critical density with an even finer microstructure. In the companion paper, we provide one such example using high green density (61%) to lower T_1.[14]

Lastly, we acknowledge that the discrepancy in $F(\rho)$ between our data and the previous studies makes our earlier estimate of δD_0, based on the model of Hansen *et al.*,[26] inaccurate. However, the uncertainty here is of the order of 10–50, which is well within the scatter of typical diffusion data. Therefore, our conclusion that second-step sintering proceeds by grain boundary diffusion should remain valid.

V. Conclusions

1. Two-step sintering in Y_2O_3 with and without a dopant proceeds by grain boundary diffusion. The suppression of grain growth may be attributed to triple point immobility, which is facilitated by high-temperature (T_1) pre-firing.

2. Constant grain-size sintering of Y_2O_3 to nearly full density was achieved at 800°C, which is less than 0.4 of the homologous temperature. The kinetic window for second-step sintering has a characteristic shape, spanning a wider temperature range with increasing grain size. At higher temperatures, grain growth occurs, for which the driving force diminishes as grain size increases. At lower temperatures, diffusion manifests long transients and eventually comes to exhaustion especially at smaller grain sizes. Dopants may enhance or suppress the overall kinetics and shift the temperature range of the kinetic window, but not affect the above general features.

3. The pre-factor in the Herring's scaling law in constant grain size sintering follows an exponential decay. It implies a gradual increase of pore spacing. This is because pores around

larger grains are more difficult to sinter, and they become dominant later.

4. Applying two-step sintering to Y_2O_3, a coarsening ratio of two, from powder particle size to dense ceramic grain size, was achieved using 200 nm powders. This ratio was 6 for 10 nm powders, which is still much lower than in conventional sintering. Therefore, the two-step method offers a promising approach for fabrication of bulk nanograin ceramics.

References

[1]R. L. Coble and J. E. Burke, "Sintering in Ceramics"; pp. 197–251 in *Progress in Ceramic Science*, Vol. 3, Edited by J. E. Burke. Pergamon Press, New York, 1963.

[2]R. J. Brook, "Controlled Grain Growth"; pp. 331–64 in *Treatise on Materials Science and Technology*, Vol. 9, Edited by F. F. Y. Wang. Academic Press, New York, 1976.

[3]R. L. Coble and R. M. Cannon, "Current Paradigms in Powder Processing," *Mater. Sci. Res*, **11**, 151 (1978).

[4]R. L. Coble, H. Song, R. J. Brook, C. A. Handwerker, and J. M. Dynys, "Sintering and Grain Growth in Alumina and Magnesia"; pp. 839–52 in *Structure and Properties of MgO and Al_2O_3 Ceramics. Advances in Ceramics*, Vol. 10, Edited by W. D. Kingery. American Ceramic Society, Westerville, OH, 1984.

[5]C. P. Cameron and R. Raj, "Grain Growth Transition During Sintering of Colloidally Prepared Alumina Powder Compacts," *J. Am. Ceram. Soc.*, **71** [12] 1031–5 (1988).

[6]T. S. Yeh and M. D. Sacks, "Effect of Green Microstructure on Sintering of Alumina"; pp. 309–31 in *Ceramic Transactions, Vol. 7, Sintering of Advanced Ceramics*, Edited by C. A. Handwerker, J. E. Blendell, and W. A. Kaysser. American Ceramic Society, Westerville, OH, 1988.

[7]F. A. Nichols and W. W. Mullins, "Surface-(Interface) and Volume-Diffusion Contributions to Morphological Changes Driven by Capillarity," *Trans. TMS-AIME*, **233** [10] 1840–8 (1965).

[8]G. N. Hassold, I.-W. Chen, and D. J. Srolovitz, "Computer Simulation of Final-Stage Sintering: I. Model, Kinetics, and Microstructure," *J. Am. Ceram. Soc.*, **73** [10] 2857–64 (1990).

[9]I.-W. Chen, G. N. Hassold, and D. J. Srolovitz, "Computer Simulation of Final-Stage Sintering: II. Influence of Initial Pore-Size," *J. Am. Ceram. Soc.*, **73** [10] 2865–72 (1990).

[10]R. L. Coble, "Sintering Crystalline Solids. I. Intermediate and Final State Diffusion Models," *J. Appl. Phys.*, **32** [5] 787–92 (1961).

[11]R. L. Coble, "Sintering Crystalline Solids. II. Experimental Test of Diffusion Models in Powder Compacts," *J. Appl. Phys.*, **32** [5] 793–9 (1961).

[12]I.-W. Chen and X.-H. Wang, "Sintering Dense Nanocrystalline Oxide Without Final Stage Grain Growth," *Nature*, **404**, 168–71 (2000).

[13]W. D. Kingery and B. Francois, "The Sintering of Crystalline Oxides, I. Interaction Between Grain Boundaries and Pores," p. 471 in *Sintering and Related Phenomena*, Edited by G. C. Kuczynski, N. S. Hooton, and C. F. Gibbon. Gordon and Breach, New York, 1967.

[14]X.-H. Wang, X.-Y. Deng, H.-L. Bao, H. Zhou, W.-G. Qu, L.-T. Li, and I.-W. Chen, "Two-Step Sintering of Ceramics with Constant Grain Size, II. $BaTiO_3$ and Ni–Cu–Zn Ferrite," *J. Am. Ceram. Soc.*, **89** [2] 438–43 (2006).

[15]P. Duran, F. Capel, J. Tartaj, C. Moure, "A Strategic Two-Stage Low-Temperature Thermal Processing Leading to Fully Dense and Fine-Grained Doped-ZnO Varistors," *Adv. Mater.*, **14** [2] 137 (2002).

[16]Y-I. Lee, Y-W. Kim, M. Mitomo, and D-Y. Kim, "Fabrication of Dense Nanostructures Silicon Carbide Ceramics Through Two-Step Sintering," *J. Am. Ceram. Soc.*, **86** [10] 1803 (2003).

[17]W. D. Kingery and M. Berg, "Study of Initial Stages of Sintering Solid by Viscous Flow, Evaporation-Condensation and Self-Diffusion," *J. Appl. Phys.*, **26** [10] 1205–12 (1955).

[18]R. L. Coble, "Intermediate-Stage Sintering: Modification and Correction of a Lattice Diffusion Model," *J. Appl. Phys.*, **36**, 2327 (1965).

[19]D. L. Johnson, "New Methods of Obtaining Volume, Grain Boundary, and Surface Diffusion Coefficients from Sintering Data," *J. Appl. Phys.*, **40** [1] 192–200 (1969).

[20]D. L. Johnson, "A General Model for the Intermediate Stage of Sintering," *J. Am. Ceram. Soc.*, **53**, 574–7 (1970).

[21]M. F. Ashby, "A First Report on Sintering Diagrams," *Acta Metall.*, **22** [3] 275–89 (1974).

[22]F. B. Swinkels and M. F. Ashby, "A Second Report on Sintering Diagrams," *Acta Matall.*, **29** [1] 259–81 (1981).

[23]R. T. DeHoff, "A Cell Model for Microstructural Evolution During Sintering"; pp. 23–34 in *Sintering and Heterogeneous Catalysis*, Edited by G. C. Kuczynski, A. E. Miller, and G. A. Sargent. Plenum Press, New York, 1984.

[24]M.-Y. Chu, M. N. Rahaman, L. C. De Jonghe, and R. J. Brook, "Effect of Heating Rate on Sintering and Coarsening," *J. Am. Ceram. Soc.*, **74** [6] 1217–25 (1991).

[25]J. Zhao and M. P. Harmer, "Sintering Kinetics for a Model Final-Stage Microstructure: A Study in Al_2O_3," *Phil. Mag. Lett.*, **63** [1] 7–14 (1991).

[26]J. D. Hansen, R. P. Rusin, M.-H. Teng, and D. L. Johnson, "Combined Stage Sintering Model," *J. Am. Ceram. Soc.*, **75** [5] 1129–35 (1992).

[27]C. Herring, "Effect of Change of Scale on Sintering Phenomena," *J. Appl. Phys.*, **21** [4] 301–3 (1950).

[28]C. Herring, "Surface Tension as a Motivation for Sintering"; pp. 143–79 in *The Physics of Powder Metallurgy*, Edited by W. E. Kingston. McGraw-Hill, New York, 1951.

[29]J. Zhao and M. P. Harmer, "Sintering of Ultra-High Purity Alumina Doped Simultaneously with MgO and FeO," *J. Am. Ceram. Soc.*, **70** [12] 860–6 (1987).

[30]I.-W. Chen and P.-L. Chen, "Sintering Characteristics of Fine Oxide Powders"; pp. 293–330 in *Proceedings of the Korean–Japan–US Workshop on Microstructure Development in Materials, Center for Interface Science and Engineering of Materials*. Kaist, Taejon, Korea, 1996.

[31]P.-L. Chen and I.-W. Chen, "Sintering of Fine Oxide Powder: I. Microstructural Evolution," *J. Am. Ceram. Soc.*, **79** [12] 3129–41 (1996).

[32]P.-L. Chen and I.-W. Chen, "Grain Boundary Mobility in Y_2O_3: Defect Mechanism and Dopant Effects," *J. Am. Ceram. Soc.*, **79** [7] 1801–809 (1996).

[33]D. J. Sordelet and M. Akinc, "Sintering of Monosized Spherical Yttria Powder," *J. Am Ceram. Soc.*, **7** [12] 1148–53 (1988).

[34]P.-L. Chen and I.-W. Chen, "Grain Growth in CeO_2: Dopant Effects, Defect Mechanisms, and Solute Drag," *J. Am. Ceram. Soc.*, **79** [7] 1793–800 (1996).

[35]P.-L. Chen and I.-W. Chen, "Sintering of Fine Oxide Powder: II: Sintering Mechanisms," *J. Am. Ceram. Soc.*, **80** [3] 637–45 (1997).

[36]L. Czubayko, V. G. Sursaeva, G. Gottstein, and L. S. Shvindlerman, "Influence of Triple Junctions on Grain Boundary Motion," *Acta Mater.*, **46** [16] 5863–71 (1998).

[37]G. Gottstein and L. S. Shvindlerman, "Triple Junction Dragging and Von Neumann–Mullins Relation," *Scripta Mater.*, **38** [10] 1541–7 (1998).

[38]J. W. Cahn, "Theory of Crystal Growth and Interface Motion in Crystalline Materials," *Acta Metall.*, **8** [8] 554–62 (1960).

[39]B. Burton, "Interface-Reaction-Controlled Diffusional Creep, A Consideration of Grain-Boundary Dislocation Climb Sources," *Mater. Sci. Eng.*, **10** [1] 9–14 (1972).

[40]R. M. Cannon, W. H. Rhodes, and A. H. Heuer, "Plastic Deformation of Fine-Grained Alumina: I. Interface-Controlled Diffusional Creep," *J. Am. Ceram. Soc.*, **63** [1–2] 48–53 (1980).

[41]E. Arzt, M. F. Ashby, and R. A. Verrall, "Interface-Controlled Diffusional Creep," *Acta Metall.*, **31** [12] 1977–89 (1983). □